Journal of Alloys and Compounds 509 (2011) 6457–6461

Contents lists available at ScienceDirect

Journal of Alloys and Compounds

journal homepage: www.elsevier.com/locate/jallcom

Spectroscopic and upconversion properties of Er^{3+}/Yb^{3+}-codoped KLTN single crystal

Lei Li, Zhongxiang Zhou*, Lei Feng, Huan Li, Ye Wu

Department of Physics, Harbin Institute of Technology, No. 92, West Da-Zhi Street, Harbin 150001, Heilongjiang, China

ARTICLE INFO

Article history:
Received 15 December 2010
Received in revised form 14 March 2011
Accepted 16 March 2011
Available online 23 March 2011

Keywords:
Rare-earth-doped materials
Absorption and luminescence properties
KLTN crystal

ABSTRACT

A high optical quality erbium and ytterbium codoped potassium lithium tantalate niobate single crystal is grown by top-seed solution growth method, and the crystal structure is confirmed to be 4 mm point group and *P4/mbm* space group by powder X-ray diffraction analysis. The ultraviolet–visible–near infrared absorption spectrum, upconversion fluorescence spectrum excited by 975 nm continuous wave laser, power dependence, and fluorescence decay curves of Er^{3+} ions in the crystal are measured at room temperature. The Judd–Ofelt (JO) intensity parameters are calculated using the JO theory and absorption spectrum. The relationship of JO parameters $\Omega_4 < \Omega_6$ of Er^{3+} in the crystal is different from the general trend of $\Omega_2 > \Omega_4 > \Omega_6$. The absorption cross sections and emission cross sections of $^2H_{11/2}$, $^4S_{3/2}$, and $^4F_{9/2}$ levels are calculated. The upconversion mechanism of Er^{3+} in the crystal is discussed based on pump power dependence analyses and decay curves. The emission intensities exhibit quadratic behaviors against pump energy, which are verified by the deduction of transition rate equation model.

1. Introduction

In recent years, rare-earth-ion-doped frequency upconversion (UC) luminescence materials, e.g., single crystals, glass, ceramics, quantum dots, and nanocrystals, are intensively studied for the potential applications in solid-state-lasers, color displays, light-emitting diodes, and fluorescence labeling, etc. [1–8]. In these materials, Er^{3+} has been considered as an ideal blue, green, and red luminescence center due to its unique level structure. On the other hand, Yb^{3+} is widely used as the most effective sensitizing ion due to its large absorption cross section around 980 nm and effective energy transfer to luminescence center [9]. Meanwhile, Yb^{3+} is also used as an energy transfer bridging ion among multiple rare earth (RE) ions codoped system to optimize the UC emissions [10]. Therefore, much attention has been devoted to investigate Er^{3+}/Yb^{3+} codoped materials, since Yb^{3+} can obviously enhance the Er^{3+} UC emission efficiency in the system. Moreover, Yb^{3+} can modify the relative intensities of Er^{3+} green and red emissions by altering the Yb^{3+} concentration [11].

Tungsten bronze-type potassium lithium tantalate niobate $K_{1-y}Li_yTa_{1-x}Nb_xO_3$ (KLTN) single crystal is a kind of excellent nonlinear optical crystal. It can be used for blue second harmonic generation (SHG) due to its large nonlinear optical coefficients and high photorefractive resistance threshold [12]. However, the basic spectroscopic properties of RE ions doped KLTN single crystal have seldom been investigated. As far as we know, only the photoluminescence properties of Er^{3+} doped potassium tantalate niobate polycrystalline materials were reported by Wen et al. [13]. So, it is of great significance to grow the KLTN single crystal doped with RE ions and to study its luminescent properties considering its extensive research and application prospects for the UC luminescent properties.

In this paper, the single crystal of tungsten bronze-type KLTN codoped with Er^{3+} and Yb^{3+} was grown using top-seed solution growth (TSSG) method. The UV–VIS–NIR absorption spectrum of Er^{3+}/Yb^{3+}-codoped KLTN single crystal was measured, and its Judd–Ofelt (JO) parameters were calculated. The UC emission under 975 nm diode laser excitation was presented. The Er^{3+} absorption and emission cross sections were estimated based on the measured absorption and emission spectra. Spectral and pump power dependence analyses were used to clarify the UC emission mechanism. The UC emission rate equation model was built and deduced.

2. Experimental

2.1. Crystal sample preparation and structure characterization

The single crystal of $K_{0.603}Li_{0.397}Ta_{0.428}Nb_{0.572}O_3$ codoped with 0.2 mol% Er^{3+} and 0.1 mol% Yb^{3+} ions was grown in air using TSSG method. More details of crystal growth can be found in our previous report [14] and other researchers' reports [15]. The grown crystal is irregular cylinders, transparent, and pink in color. The crack-free crystal is about 5 mm in diameter. To identify the crystal structure, powder X-ray diffraction analysis (XRD) was carried out in the 2θ range from 10° to 80° using XRD-6000 Shimadzu diffractometer. The test result reveals that the crystal

* Corresponding author. Tel.: +86 451 86414141; fax: +86 451 86414141.
E-mail address: zhouzx@hit.edu.cn (Z. Zhou).

0925-8388/$ – see front matter © 2011 Elsevier B.V. All rights reserved.
doi:10.1016/j.jallcom.2011.03.094

belongs to tetragonal tungsten bronze-type structure with the 4 mm point group and *P*4/*mbm* space group. The unit cell parameters are $a = b = 12.53$ Å, and $c = 3.92$ Å. Its Curie temperature (T_c) was tested to be 271 °C by the differential thermal analysis (DTA). The sample was cut from the grown crystal and polished to optical grade for optical measurements.

2.2. Spectroscopic characterization

UV–VIS–NIR absorption spectra of Er^{3+}/Yb^{3+}-codoped KLTN crystal was measured in the wavelength range of 350–1650 nm with an unpolarized light vertical to the sample and nothing was equipped in the reference arm of Perkin-Elmer Lambda 950 spectrophotometer. The scanning step and scanning speed were fixed at 2 nm and 300 nm/min, respectively. The surface reflection and host absorption of the sample were neglected during optical absorption measurement.

The sample was utilized for spectral studies by irradiation with a focused 500 mW power-controllable 975 nm diode laser (Hi-Tech Optoelectronics Co., Ltd.), and the emitted UC fluorescence was collected by a lens-coupled monochromator (Zolix instruments Co., Ltd.) attached to a photomultiplier (Hamamatsu CR 131). Finally, the spectrum data were acquired through a desktop computer. The scanning wavelength range was from 400 nm to 900 nm and scanning step was 0.5 nm. The pump power dependence of the 548 and 665 nm emissions were measured by alteration of the electric current input to the 975 nm laser diode, and the integrated intensities of the emission bands were calculated. In the measurement of decay profiles about 548 and 665 nm emissions, the 975 nm laser diode was modulated by a square-wave electric current with the repeat frequency 50 Hz, and the falling edges were recorded via a Tektronix TDS 5052 digital oscilloscope. All the measurements were performed at room temperature.

3. Results and discussion

3.1. Absorption spectrum

Absorption spectrum of the sample is shown in Fig. 1. Taking into account the description of the optical and luminescence transitions of Er^{3+} and Yb^{3+} in multiple host, all the transitions of Er^{3+} and Yb^{3+} in KLTN host are found in the range of 350–1650 nm. The corresponding transitions of the absorption bands from the ground state to the excited states are listed in the figure. We measured the absorption spectrum of single doped Er^{3+} ions with the same mole concentration in KLTN crystal, and presented the 980 nm absorption band in the inset. As is illustrated, the absorption integrated cross section of the Yb^{3+} ions $^2F_{5/2}$ level is about ten times bigger than that of Er^{3+} ions $^4I_{11/2}$ level, implying that the Yb^{3+} ions have higher absorption efficiency than Er^{3+} ions around 980 nm. The standard JO theory has been extensively used to analyze the spectroscopic properties of RE ions doped crystals and glass [16–19].

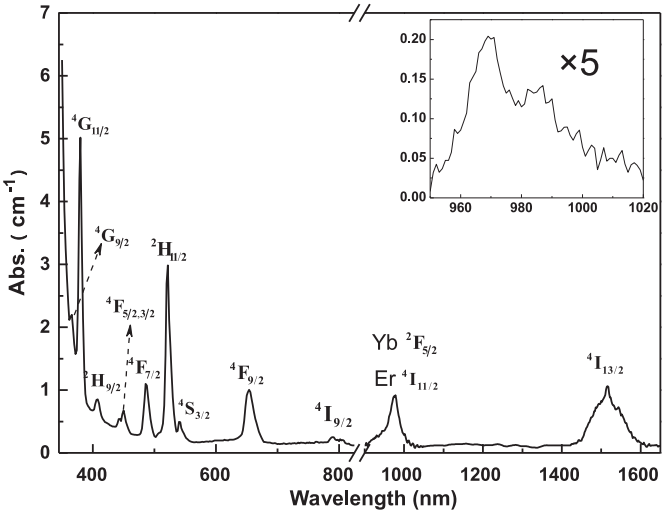

Fig. 1. UV–VIS–NIR absorption spectrum of KLTN crystal codoped with 0.2 mol% Er^{3+} and 0.1 mol% Yb^{3+}, the assignments of absorption peaks corresponding transitions from ground state are listed. The inset shows Er^{3+} absorption band of transition $^4I_{15/2} \rightarrow {}^4I_{11/2}$ in 0.2 mol% Er^{3+}:KLTN crystal.

It has been depicted in some literatures, so only the calculated JO intensity parameters and root mean-square deviation of KLTN crystal are given as below:

$$\Omega_2 = 3.13 \times 10^{-19}\ \text{cm}^2, \quad \Omega_4 = 1.16 \times 10^{-19}\ \text{cm}^2,$$
$$\Omega_6 = 1.49 \times 10^{-19}\ \text{cm}^2, \quad \text{and} \quad \delta_{\text{rms}} = 6.55 \times 10^{-6}.$$

The 980 nm absorption band corresponding to the $^4I_{11/2}$ level of Er^{3+} ions is neglected in the calculation since it is interfered by the $^2F_{5/2}$ level absorption of Yb^{3+} ions. The value relationship of $\Omega_4 < \Omega_6$ differs from the general trend of $\Omega_2 > \Omega_4 > \Omega_6$ for Er^{3+} ions. The Ω_2 parameter is the most sensitive to local crystal field and it is correlated with the degree of covalence [20], hence the larger Ω_2 value is due to the strong covalent bond of the Er^{3+} ions with their ligands. In addition, the strong covalent nature is responsible for the larger oscillator strengths than those of other materials [21,22]. Another possible reason is that the segregation phenomenon of Er^{3+} is serious in the crystal growth process. The segregation coefficients of Er^{3+} are bigger than 1.0, which leads to the larger actual Er^{3+} concentrations in crystal than the theoretical values, so the calculated JO parameters are bigger than the ideal values. Based on these JO line strengths, the probability for spontaneous emission from an excited manifold J to a lower manifold J' can be calculated. The calculated spontaneous emission probabilities of Er^{3+} ions $^4F_{9/2}$ and $^4S_{3/2}$ levels are $A_4 = 5.591 \times 10^4\ \text{s}^{-1}$ and $A_3 = 3.383 \times 10^4\ \text{s}^{-1}$, respectively.

The absorption cross-section at various wavelengths can be calculated by the formula [19]:

$$\sigma_{\text{abs}}(\lambda) = \frac{\alpha(\lambda)}{N} = \frac{\ln\left[I_{\text{a0}}(\lambda)/I_{\text{a}}(\lambda)\right]}{Nd} = \frac{OD(\lambda)\ln(10)}{Nd}, \quad (1)$$

where N is the number density and d is the thickness of sample. $I_{\text{a0}}(\lambda)$ and $I_{\text{a}}(\lambda)$ are the incident and transmitted light intensities of the sample in the absorption spectrum measurement. The calculated absorption cross-section line shape for the transitions from $^4I_{15/2}$ to $^2H_{11/2}$, $^4S_{3/2}$, and $^4F_{9/2}$ levels is presented in Fig. 3.

3.2. UC emissions

Fig. 2 shows the UC emissions of Er^{3+}/Yb^{3+}-codoped KLTN crystal under the excitation of 975 nm laser. Three emission bands peaking at 548 nm (green), 665 nm (red), and 850 nm are observed, which correspond to the Er^{3+} ions transitions of $^4S_{3/2} \rightarrow {}^4I_{15/2}$,

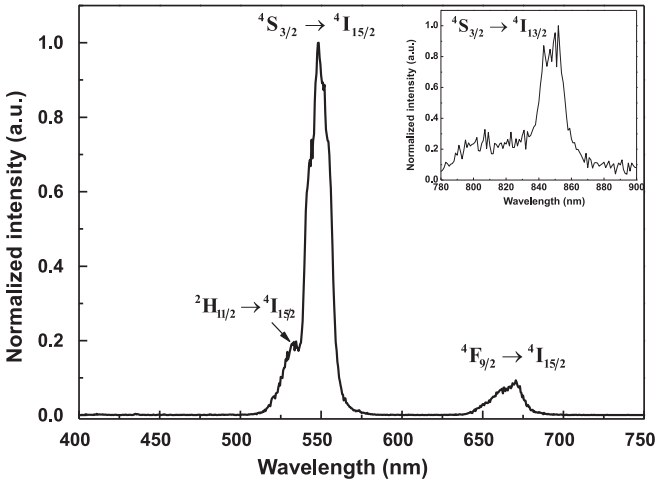

Fig. 2. UC fluorescence spectrum of Er^{3+}/Yb^{3+}-codoped KLTN single crystal under 975 nm laser excitation. The inset shows the 850 nm UC emission band. The transitions corresponding emission bands are listed in the inset.

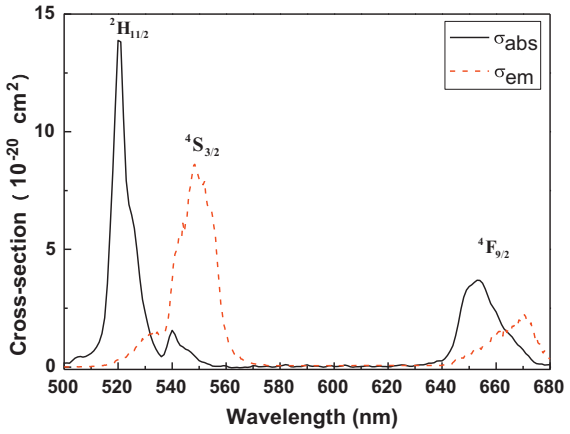

Fig. 3. Absorption and emission cross section line shapes for Er^{3+} levels in Er^{3+}/Yb^{3+}-codoped KLTN single crystal.

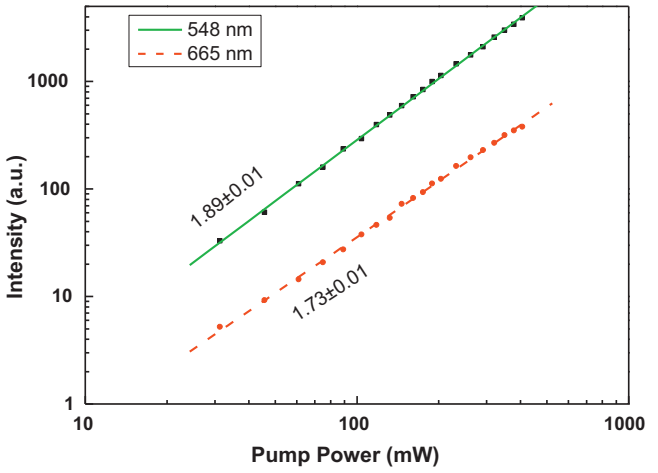

Fig. 4. Double logarithmic plot of pump power dependence of UC luminescence bands centered at 548 and 665 nm after excitation at 975 nm for Er^{3+}/Yb^{3+}-codoped KLTN single crystal.

$^4F_{9/2} \rightarrow {}^4I_{15/2}$, and $^4S_{3/2} \rightarrow {}^4I_{13/2}$, respectively. This result has been observed in many types of host including crystals and glass. The stimulated emission cross-section can be calculated from the room temperature UC emission spectrum using the Füchtbauer–Landenburg method [16,23]:

$$\sigma_{em}(\lambda) = \frac{A\lambda^5 I(\lambda)}{8\pi c n^2 \int \lambda I(\lambda) d\lambda}, \quad (2)$$

where $I(\lambda)$ is the measured intensity of the emission spectrum, A is the spontaneous emission probability calculated by JO theory, and n is the refractive index. The calculated emission cross-section line shapes for the transitions $^2H_{11/2}/^4S_{3/2} \rightarrow {}^4I_{15/2}$ and $^4F_{9/2} \rightarrow {}^4I_{15/2}$ are presented in Fig. 3. It can be seen that Er^{3+} in KLTN exhibits large $^2H_{11/2}$ level absorption cross-section and $^4S_{3/2}$ level emission cross-section, and the emission cross-sections have obviously red shift compared with the corresponding absorption cross-sections. The peak stimulated emission cross-section at 548 nm is 8.6×10^{-20} cm^2, which is one order of magnitude larger than that in Er^{3+}:$LiNbO_3$ crystal, e.g., 8.8×10^{-21} cm^2 in Ref. [24], with effective line width of 17 nm. Moreover, the lower crystal symmetry of KLTN crystal leads to broad Er^{3+} emission bands in this system, which provides opportunities for tunable wavelength laser design.

Pump dependence of green and red UC fluorescence in KLTN crystal are investigated. For an unsaturated UC process, it is well known that the number of photons that are required to populate the upper emission state can be obtained by the following relation [9]:

$$I_f \propto P^n, \quad (3)$$

where I_f is the fluorescent intensity, P is the pump laser power, and n is the number of the laser photons required. As shown in Fig. 4, the n values for green and red UC emissions in Er^{3+}/Yb^{3+}-codoped KLTN crystal are 1.89 and 1.73, which means that two-photon processes are involved to populate the Er^{3+} ions $^4S_{3/2}$ and $^4F_{9/2}$ states. These n values achieved here are similar to those in other samples presented, which are not shown here.

In order to further understand the UC mechanism, the decay kinetics of green and red emission is investigated. The semilogarithmic normalized decay profiles of $^4S_{3/2} \rightarrow {}^4I_{15/2}$ and $^4F_{9/2} \rightarrow {}^4I_{15/2}$ transitions centered at 548 nm and 665 nm in the KLTN crystals doped with 0.2 mol% Er^{3+} ions and codoped with 0.2 mol% Er^{3+}/0.1 mol% Yb^{3+} ions are shown in Fig. 5. The decay profiles of green and red emissions can be best fitted by a biexponential function instead of a single exponential for these samples. The fitting biexponential function can be expressed as [10]:

$$I(t) = A \exp\left(-\frac{t}{\tau_s}\right) + B \exp\left(-\frac{t}{\tau_l}\right) + I_0. \quad (4)$$

The first term in Eq. (4) is the contribution of the quick decay process with a lifetime of τ_s, the second term is the contribution of slow decay process with a lifetime of τ_l, and the third term is the background noise. Effective lifetime (τ_m) is usually defined as [25]:

$$\tau_m = \frac{\int_0^\infty tI(t)dt}{\int_0^\infty I(t)dt}. \quad (5)$$

The obtained fitting parameters are listed in Table 1. The short lifetimes arise from the direct decay from the Er^{3+} ions $^4S_{3/2}$ and $^4F_{9/2}$ states, while the long lifetimes arise from the energy transfer (ET) process from the intermediate states of $^2F_{5/2}$ (Yb^{3+}) to $^4I_{11/2}$ and $^4I_{13/2}$ (Er^{3+}). The ratio of B to A (B/A) expresses the proportion of two processes. By doping Yb^{3+} ions into the sample, the lifetime of 548 nm green emissions is extended because the lifetime of the Yb^{3+} ions $^2F_{5/2}$ level is longer than that of the Er^{3+} ions $^4S_{3/2}$ level. Meanwhile, the lifetime of 665 nm red emissions becomes shorter, which may be caused by an effective energy back transfer process from Er^{3+} to Yb^{3+} ions [$Yb(^2F_{7/2}) + Er(^4S_{3/2}) \rightarrow Yb(^2F_{5/2}) + Er(^4I_{13/2})$] [26]. It can be confirmed that the ET process from Yb^{3+} ions to Er^{3+} ions plays an important role in the UC emissions. Since the population inversion is easily implemented in laser system due to the long level lifetime, it is expected that the Er^{3+}/Yb^{3+}-codoped KLTN can be used as a new kind of laser crystal.

Fig. 6 shows the energy level diagrams of Er^{3+} and Yb^{3+} ions, as well as the proposed mechanism to produce the green and red fluorescence [27]. The Er^{3+} ions are firstly excited from ground state to

Table 1
Decay times of green and red emissions in 0.2 mol% Er^{3+}:KLTN and 0.2 mol% Er^{3+}/0.1 mol% Yb^{3+} codoped KLTN crystals fitting based on Eqs. (4) and (5).

Emission bands	Sample	τ_s (μs)	τ_l (μs)	B/A	τ_m (μs)
Green	Er^{3+}:KLTN	160	330	0.54	248
	Er^{3+}/Yb^{3+}:KLTN	107	323	0.83	258
Red	Er^{3+}:KLTN	134	616	5.66	568
	Er^{3+}/Yb^{3+}:KLTN	203	530	6.42	501

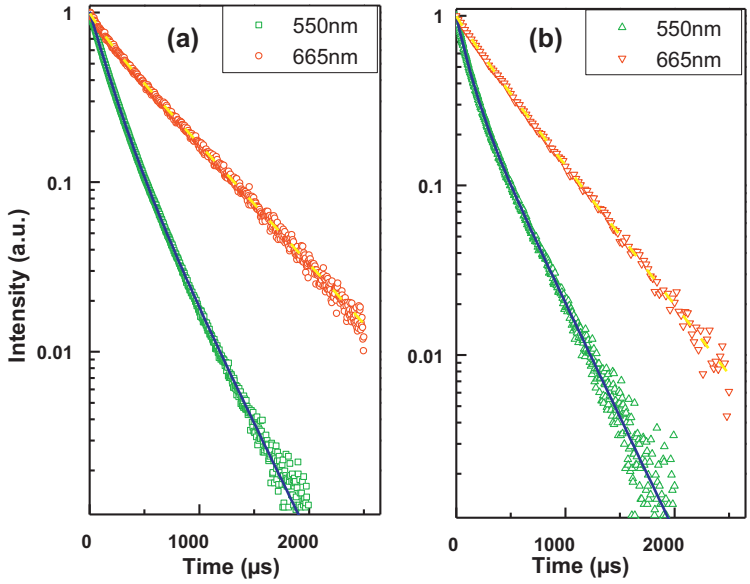

Fig. 5. Semilogarithmic decay profiles of Er^{3+} at 550 nm and 665 nm after 975 nm LD laser excitation of 0.2 mol% Er^{3+} doped (a) and 0.2 mol% Er^{3+} and 0.1 mol% Yb^{3+} codoped (b) KLTN crystals.

$^4I_{11/2}$ level by ground state absorption (GSA) or energy transfer [ET1 : $Yb(^2F_{5/2}) + Er(^4I_{15/2}) \rightarrow Yb(^2F_{7/2}) + Er(^4I_{11/2})$] processes, and then to $^4F_{7/2}$ level via the excited state absorption (ESA) or energy transfer [ET2 : $Yb(^2F_{5/2}) + Er(^4I_{11/2}) \rightarrow Yb(^2F_{7/2}) + Er(^4F_{7/2})$] processes. The ions at the $^4F_{7/2}$ level undergo a multi-phonon assisted relaxation to $^4S_{3/2}/^2H_{11/2}$ levels, and mostly populate in the $^4S_{3/2}$ level, from which the green UC emission arises. The ions at $^4I_{11/2}$ level relax to $^4I_{13/2}$ level by multi-phonon assist; moreover, the ions at $^4S_{3/2}$ level undergo the above-mentioned energy back transfer process [ET4] and relax to $^4I_{13/2}$ level. And then they are excited to $^4F_{9/2}$ level via ESA or ET3 [$Yb(^2F_{5/2}) + Er(^4I_{13/2}) \rightarrow Yb(^2F_{7/2}) + Er(^4F_{9/2})$] processes, from which the red UC emission arises.

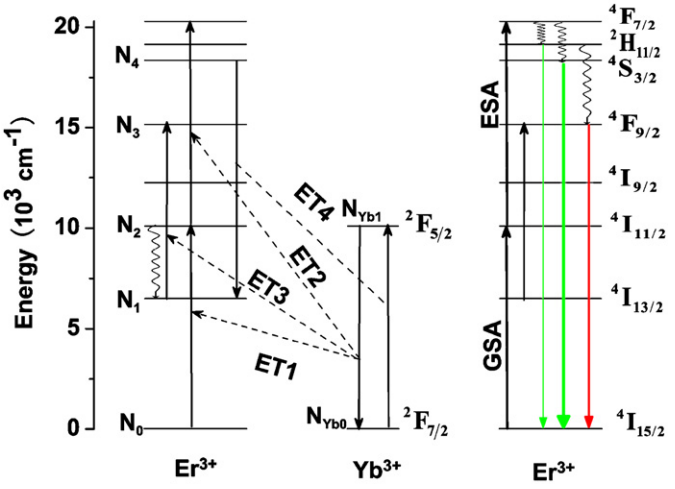

Fig. 6. Schematic UC emission processes under 975 nm excitation proposed for Er^{3+}/Yb^{3+}-codoped KLTN single crystal. Radiative transition, ET, and multi-phonon relaxation are denoted by solid, dashed, and jagged arrows, respectively.

In order to make a general theoretically description for the green and red UC emissions, we derive the rate equations according to Ref. [28].

$$\frac{dN_1}{dt} = W_{41}\frac{N_4}{N_{RE}}N_{Yb0} + W_{21}N_2 - W_{13}\frac{N_{Yb1}}{N_{RE}}N_1 - A_{13}N_1 - \frac{N_1}{\tau_1}, \quad (6)$$

$$\frac{dN_2}{dt} = W_{02}\frac{N_{Yb1}}{N_{RE}}N_0 + A_{02}N_0 - W_{24}\frac{N_{Yb1}}{N_{RE}}N_2 - W_{21}N_2 - A_{24}N_2 - \frac{N_2}{\tau_2}, \quad (7)$$

$$\frac{dN_3}{dt} = W_{13}\frac{N_{Yb1}}{N_{RE}}N_1 + W_{43}N_4 + A_{13}N_1 - \frac{N_3}{\tau_3}, \quad (8)$$

$$\frac{dN_4}{dt} = W_{24}\frac{N_{Yb1}}{N_{RE}}N_2 + A_{24}N_2 - W_{41}\frac{N_4}{N_{RE}}N_{Yb0} - W_{43}N_4 - \frac{N_4}{\tau_4}, \quad (9)$$

$$\frac{dN_{Yb1}}{dt} = \rho\sigma_{Yb}N_{Yb0} + W_{41}\frac{N_4}{N_{RE}}N_{Yb0} - (W_{02}N_0 + W_{13}N_1 + W_{24}N_2)\frac{N_{Yb1}}{N_{RE}} - \frac{N_{Yb1}}{\tau_{Yb}}, \quad (10)$$

and

$$\beta_{green} = \frac{\tau_4}{\tau_{rad}} \quad (11)$$

where $N_i(W_{ji}, A_{ji}, \tau_i)$ ($i = 0, 1, 2, 3, 4$; $j = 0, 1, 2, 3, 4$) are the population densities (ET rates from j state to i state, ESA or GSA rates from j state to i state, and decay time) of the $^4I_{15/2}$, $^4I_{13/2}$, $^4I_{11/2}$, $^4F_{9/2}$, and $^4S_{3/2}$ states of the Er^{3+} ions, respectively; N_{Yb0} and N_{Yb1} are the population densities of Yb^{3+} ions in the ground and excited states, respectively; N_{RE} is the sum of the rare-earth concentrations in crystal; ρ is the laser photon number density; σ_{Yb} denotes the absorption cross section of Yb^{3+} ion; τ_{Yb} and τ_{rad} are radiation lifetimes of $^2F_{5/2}$ and $^4S_{3/2}$ states; β_{green} and β_{red} are the luminescent population ratios in $^4S_{3/2}$ and $^4F_{9/2}$ states, respectively. In the steady-state condition, Eqs. (6)–(10) all equal to zero. The $W_{41}(N_4/N_{RE})N_{Yb0}$ term in Eq. (10) is neglected in the following discussions since its contribution to N_{Yb1} is much smaller than that

induced by laser population [27]. Furthermore, the UC rates are supposed to be much lower than their decay rates and are neglected in the deduction process [29]. According to Eqs. (6)–(11), a general theoretical description of the fluorescent radiation intensity is shown as:

$$I_{\text{green}} = \frac{N_4 h\nu_{\text{green}}}{\tau_{\text{rad}}} = \frac{\beta_{\text{green}} N_4 h\nu_{\text{green}}}{\tau_4}$$

$$= \beta_{\text{green}} h\nu_{\text{green}} W_{02} W_{24} N_0 \tau_2 \tau_{\text{Yb}}^2 \rho^2 \left(\frac{\sigma_{\text{Yb}} N_{\text{Yb0}}}{N_{\text{RE}}}\right)^2 \propto \rho^2, \quad (12)$$

and

$$I_{\text{red}} = I - I_{\text{green}} = \frac{I(1-\beta_{\text{green}})}{\beta_{\text{green}}} \propto \rho^2. \quad (13)$$

Eqs. (12) and (13) indicate that the green and red emissions will have a quadratic power dependence on the laser power, which coincides well with the conclusion of the pump power dependence analyses.

4. Conclusions

An Er^{3+}/Yb^{3+}-codoped KLTN single crystal with tetragonal tungsten bronze-type structure was grown by TSSG method. Typical absorption bands of Er^{3+} and Yb^{3+} ions were revealed by the UV–VIS–NIR absorption spectrum. The calculated JO intensity parameters are $\Omega_2 = 3.57 \times 10^{-19}$ cm^2, $\Omega_4 = 0.93 \times 10^{-19}$ cm^2, and $\Omega_6 = 1.56 \times 10^{-19}$ cm^2. The parameter Ω_2 is the largest, which manifests that Er^{3+} ions are in a strongly polarized environment. Green and red UC emissions are observed under 975 nm excitation, both of which are two-photon processes. The calculated emission cross-sections have obviously red shift compared with the corresponding absorption cross-sections. The ET process from Yb^{3+} ions to Er^{3+} ions plays an important role in the UC emissions. At last, considering their long level lifetimes, we expect that Er^{3+}/Yb^{3+}-codoped KLTN can be used as novel laser crystal.

Acknowledgement

This work is funded by the National Natural Science Foundation of China under Project No. 50902034.

References

[1] S. Du, J. Xu, X. Dong, J. Zhang, Z. Fu, Z. Dai, J. Lumin. 130 (2010) 872.
[2] J. Cao, Y. Wang, X. Ma, J. Li, Z. Zhu, Z. You, F. Yang, C. Sun, T. Cao, Y. Ji, C. Tu, J. Alloys Compd. 509 (2011) 185.
[3] J. Ding, Q. Zhang, J. Chen, X. Liu, G. Lin, J. Qiu, D. Chen, J. Alloys Compd. 495 (2010) 205.
[4] H. Gong, D. Yang, X. Zhao, E.Y.B. Pun, H. Lin, Opt. Mater. 32 (2010) 554.
[5] S. Lu, Q. Yang, B. Zhang, H. Zhang, Opt. Mater. 33 (2011) 746.
[6] X. Hou, S. Zhou, T. Jia, H. Lin, H. Teng, J. Alloys Compd. 509 (2011) 2793.
[7] Q. Zhang, J. Ding, Y. Shen, D. Chen, Q. Zhou, Q. Chen, Z. He, J. Qiu, J. Alloys Compd. 508 (2010) L13.
[8] X. Qin, G. Zhou, H. Yang, Y. Yang, J. Zhang, S. Wang, J. Alloys Compd. 493 (2010) 672.
[9] X. Qiao, X. Fan, Z. Xue, X. Xu, Q. Luo, J. Alloys Compd. 509 (2011) 4717.
[10] A. Li, Z. Zheng, Q. LÜ, L. Sun, Y. Xu, W. Liu, W. Wu, Y. Yang, T. LÜ, J. Appl. Phys. 104 (2008) 063526.
[11] G.Y. Chen, Y.G. Zhang, S. Gomesfalean, Z.G. Zhang, Appl. Phys. Lett. 89 (2006) 163105.
[12] Y. Furukawa, S. Makio, T. Miyai, M. Sato, Appl. Phys. Lett. 68 (1996) 744.
[13] C. Wen, S. Chu, Y. Shin, C. Lee, Y. Juang, J. Alloys Compd. 459 (2008) 107.
[14] L. Li, Z. Zhou, H. Tian, D. Gong, Z. Yang, Y. Yang, J. Appl. Phys. 108 (2010) 043520.
[15] S. Podlojenov, M. Burianek, M. Mühlberg, Cryst. Res. Technol. 38 (2003) 1015.
[16] B. Zhou, E.Y. Pun, H. Lin, D. Yang, L. Huang, J. Appl. Phys. 106 (2009) 103105.
[17] K. Liu, E.Y. Pun, J. Alloys Compd. 470 (2009) 340.
[18] A.M. Babu, B.C. Jamalaiah, T. Sasikala, S.A. Saleem, L.R. Moorthy, J. Alloys Compd. 509 (2011) 4743.
[19] J. Xie, Q. Zhang, Y. Zhuang, X. Liu, M. Guan, B. Zhu, R. Yang, J. Qiu, J. Alloys Compd. 509 (2011) 3032.
[20] W. Wang, Y. Xu, C. Shen, Q. Yan, H. Zeng, G. Chen, J. Alloys Compd. 490 (2010) L37.
[21] D. Zhang, P. Hua, J. Appl. Phys. 101 (2007) 053523.
[22] E. Cantelar, M. Quintanilla, F. Cussó, E. Cavalli, M. Bettinelli, J. Phys.: Condens. Matter 22 (2010) 215901.
[23] Q. Dong, G. Zhao, J. Chen, Y. Ding, B. Yao, Z. Yu, Opt. Mater. 32 (2010) 873.
[24] A. Li, L. Sun, Z. Zheng, W. Liu, W. Wu, Y. Yang, T. Lv, Appl. Phys. A 89 (2007) 1005.
[25] R. Martínez, A.C. Lira, A. Speghini, C. Falcony, U. Caldiño, J. Alloys Compd. 509 (2011) 3160.
[26] A.M. Pires, O.A. Serra, S. Heer, H.U. Güdel, J. Appl. Phys. 98 (2005) 063529.
[27] G. Chen, H. Liu, H. Liang, G. Somesfalean, Z. Zhang, J. Phys. Chem. C 112 (2008) 12030.
[28] M. Tsuda, K. Soga, H. Inoue, S. Inoue, A. Makishima, J. Appl. Phys. 85 (1999) 29.
[29] M. Pollnau, D.R. Gamelin, S.R. Lüthi, H.U. Güdel, Phys. Rev. B 61 (2000) 3337.